Received: 28 August 2019 | Revised: 27 December 2019 | Accepted: 7 January 2020
DOI: 10.1002/er.5228

INTERNATIONAL JOURNAL OF ENERGY RESEARCH WILEY

RESEARCH ARTICLE

Equivalent circuit representation of a vortex-induced vibration-based energy harvester using a semi-empirical lumped parameter approach

Junlei Wang[1,2] | **Lihua Tang**[2] | **Liya Zhao**[3] | **Guobiao Hu**[2] | **Rujun Song**[4] | **Kun Xu**[5]

[1]Engineering Research Center of Energy Saving Technology and Equipment of Thermal Energy System, Ministry of Education, Zhengzhou University, Zhengzhou, China

[2]Department of Mechanical Engineering, The University of Auckland, Auckland, New Zealand

[3]School of Mechanical and Mechatronic Engineering, Faculty of Engineering and Information Technology, University of Technology Sydney, Ultimo, New South Wales, Australia

[4]School of mechanical engineering, Shandong University of Technology, Zibo, China

[5]Key Laboratory of Urban Security and Disaster Engineering of Ministry of Education, Beijing University of Technology, Beijing, China

Correspondence
Liya Zhao, School of Mechanical and Mechatronic Engineering, Faculty of Engineering and Information Technology, University of Technology Sydney, 15 Broadway, Ultimo 2007, New South Wales, Australia.
Email: liya.zhao@uts.edu.au

Kun Xu, Key Laboratory of Urban Security and Disaster Engineering of Ministry of Education, Beijing University of Technology, Beijing 100124, China.
Email: xukun@bjut.edu.cn

Funding information
National Natural Science Foundation of China, Grant/Award Numbers: 51708011, 51705296, 51977196, 51606171; University of Technology Sydney, Grant/Award Number: 321720.2232432; China Postdoctoral Science Foundation, Grant/Award Number: 2019M652565

Summary

Small-scale wind energy harvesting from vortex-induced vibrations (VIV) has been introduced in recent years as a renewable power source for microelectronics and wireless sensors. Previous studies have focused on modeling and optimizing the VIV-based piezoelectric energy harvester (VIVPEH) structures and simplified the complicated interface circuits as pure resistors with an alternating current (AC) output. In practice, an AC output is required to be transformed into a direct current (DC) followed by further regulations before being used for real applications. Incorporating the rectification and regulation, traditional theoretical and numerical models will become extremely cumbersome and even impossible. To address this issue, this work proposes an equivalent circuit model (ECM) for a typical VIVPEH. The Scanlan-Ehsan aerodynamic force model is employed to describe the fluid-structure interaction. Wind tunnel experiments are carried out to validate the derived model. The performances of the VIVPEH with AC and DC interface circuits are subsequently analyzed and compared to understand the influences of these circuits on the operational wind speed bandwidth, power output, vibration amplitude, and electrical damping.

KEYWORDS
equivalent circuit representation, piezoelectric, vortex-induced vibrations, wind energy harvesting

1 | INTRODUCTION

In the context of growing awareness of energy saving, emission reduction, and environmental protection, seeking more diversified clean energy sources has aroused increasing concerns from both industry and academia. Researchers have explored harvesting energy from environmental vibrations in recent years. The goal of energy harvesting is to supply energy for the low-power microelectronic systems, for example, the wireless sensor networks (WSNs) and micro-electromechanical systems (MEMS).[1] The advantage of energy harvesting lies in its sustainability and beneficial avoidance of battery replacement.[2,3] Harvesting environmental vibrations can be generally divided into two categories, that is, the preexisting base excitations resulting from the motion of machinery, structures, or human movements[4,5] and the flow-induced vibrations due to aeroelastic instabilities, such as vortex-induced vibration (VIV),[6] galloping,[7,8] flutter,[9,10] and buffeting,[11] or their synergetic effect.[12,13]

Wind energy is a steady and pervasive power source in the environment. VIV is a typical aeroelastic phenomenon resulting from periodic vortex shedding. Bernitsas and Raghavan[14,15] initially presented a mechanism that harvests energy from VIV in 2008, that is, the Vortex-induced Vibration for Aquatic Clean Energy (VIVACE). The Marine Renewable Energy Laboratory (MRELab) further developed the VIVACE to harvest the hydrokinetic power using the electromagnetic transduction. In recent years, energy harvesting technologies such as electromagnetic,[16] dielectric,[17,18] and triboelectric[19-21] have been reported by researchers, besides which piezoelectric energy harvesting has been studied widely because of its high voltage output, high power density, and ease of miniaturization.[22-30] Dai et al[31] presented a theoretical model for a linear VIV-based piezoelectric energy harvester (VIVPEH), where the wake oscillator model was employed to formulate the vortex-induced aerodynamic force acting on the cylinder. However, such a model can only be used for a smooth cylinder. To calculate the time-varying air force, Mehmood et al[32] used an “O”-type grid in CFD to solve the governing equations of the fluid flow for a VIVPEH. Zhou and Wang[33,34] used the Lattice Boltzmann method to account for the fluid-structure coupling effect together with the electromechanical equations.

On the other hand, the electrical interface circuit plays a crucial role in energy harvesting power regulation and enhancement.[22,35-38] However, the theoretical and numerical models in the previous studies are difficult to be extended to incorporate the complex coupling between the nonlinear aerodynamic force, piezoelectric and mechanical structure, and the nonlinear power extraction circuit. Recently, researchers have utilized the equivalent circuit model (ECM) to connect the structural modeling and electrical simulation based on the similar characteristics as the Van-der Pol model in an electric circuit. Yang and Tang[39] established the ECM considering multiple modes for modeling a multiple degree-of-freedom piezoelectric energy harvester under the base excitation. Bayik et al[40] developed the ECM of an energy harvester consisting of a piezoelectric patch attached to a thin plate. Silva et al[41] presented a general equivalent circuit framework for analyzing the dynamic behaviors of piezoelectric structures. Furthermore, for a wind piezoelectric energy harvesting system based on galloping, Tang et al[42] presented the ECM model by representing the linear and nonlinear aerodynamic force of galloping with an arbitrary source, which enables the system-leveled simulation integrating the aero-electro-mechanical harvester and the advanced power extraction interface circuit. Based on this model, Zhao et al[43] and Zhao and Yang[44] further investigated the power enhancement of a galloping-based wind energy harvester using the synchronized switching harvesting on inductor (SSHI) and the synchronized charge extraction (SCE) circuits. However, very little effort has been devoted to enhancing the power extraction of VIVPEHs with more sophisticated interfaces, due to the lack of an ECM that could model the aero-electro-mechanical coupled dynamics linking the vortex shedding and practical circuit.

In this paper, we employ a Scanlan-Ehsan vortex-induced vibration model[45] to represent the aerodynamic force during VIV and develop an ECM that enables system-level simulation of the coupled aero-electro-mechanical dynamics with AC and DC interface circuits. Wind tunnel experiment is conducted to identify the nonlinear aerodynamic coefficients and validate the model predictions. Both AC and DC circuits are investigated for performance comparisons. To our best knowledge, this is the first time that a VIVPEH is evaluated with a rectifying DC interface circuit. The proposed model brings much convenience for the system-level evaluation of the coupled dynamics of VIVPEHs connected with practical circuits.

2 | MECHANISM OF VIV

Vortex-induced vibrations (VIV) are induced by alternating near-wall vortex shedding from the surface of a bluff body. Figure 1 shows the typical single degree-of-freedom (SDOF) model to describe the cross-flow motion of a circular cylinder that is mounted on a spring and placed in a two-dimensional flow field with uniform velocities. When the wind passes over the bluff body, Von Kármán vortices are generated, resulting in unbalanced forces on the bluff body. In one or more narrow ranges of wind speed, resonance occurs when the vortex shedding frequency is close to the natural frequency of the system,[6,46] and large-amplitude cross-flow vibrations are induced since the supporting spring allows plunging motions. When the resonance happens, the vibration frequency is locked at the natural frequency in a specific range of wind speed, which is called the “lock-in” region. Such feature of VIV has a potential benefit in energy harvesting as VIV is capable of protecting itself when the

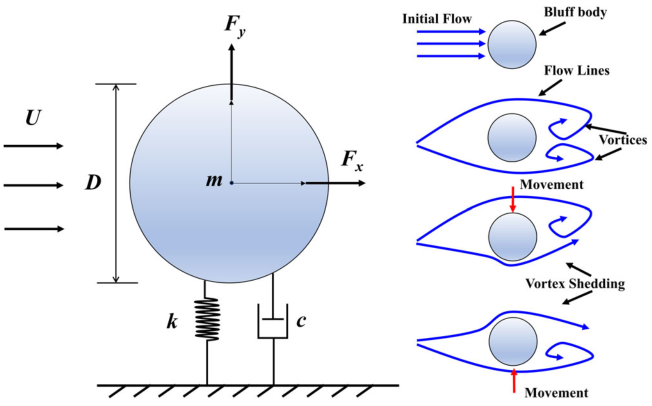

FIGURE 1 A bluff body undergoing vortex-induced vibration [Colour figure can be viewed at wileyonlinelibrary.com]

wind speed gets too high. The aerodynamic force caused by the vortex shedding is represented by the linear and nonlinear aerodynamic damping terms which contribute to the oscillations of the bluff body. In particular, the linear damping determines the threshold wind speed of the VIV lock-in region, while the nonlinear damping controls the amplitude of the oscillations.

3 | MODELING

3.1 | VIV aerodynamic model

The governing equation of the vibration system in Figure 1 can be expressed as

$$m\left(\ddot{x}+2\zeta\omega_n\dot{x}+{\omega_n}^2x\right)=F_{air}(\ddot{x},\dot{x},x,U,t), \tag{1}$$

where m is the mass of the cylinder and ζ and ω_n are the damping ratio and the natural frequency of the structure, respectively. F_{air} is the aerodynamic force acting on the circular cylinder during VIV which can be represented by a function of the wind speed U, time t, structural vibration displacement x and velocity $\dot{x}$.

In this study, we use the Scanlan-Ehsan nonlinear semi-empirical model to represent the VIV aerodynamic force on the bluff body,[45] which has shown to be able to adequately describe the lock-in region of VIV and is given by

$$F_{air}=\frac{1}{2}\rho U^2\left(2L_{tip}D\right)\left\{\lambda_1(K)\left[1-\varepsilon(K)\frac{x^2}{D^2}\right]\frac{\dot{x}}{D}+\lambda_2(K)\frac{x}{D}+\frac{1}{2}\bar{C}_L(t)\right\}, \tag{2}$$

where D is the diameter of the circular cylinder, L_{tip} is the length of the circular cylinder, ρ is the density of air, K is the frequency defined as the dimensionless form $K=\omega D/U$, and ω is the structural vibrations frequency imposed by the aerodynamic force. The average fluctuating lift force coefficient caused by vortex shedding effect when the flow passes over cylinder is represented as $\bar{C}_L(t)$ in Equation (2). The displacement-dependent aerodynamic force during VIV can be divided into two parts, that is, the effective aeroelastic damping term and the effective aeroelastic stiffness term, with the terms λ_1, ε, and λ_2 being the coefficients of the linear damping, nonlinear damping and linear stiffness, respectively. It is worth noting that ε is always nonzero, which ensures that the vibration amplitude remains self-limited.

Note that, from the literature,[45] the vortex-shedding effect can be neglected for it is quite weak as compared with the vibration-induced aerodynamic effect in VIV, especially when the vibration amplitude is high. Omitting $\bar{C}_L(t)$, Equation (2) can then be rewritten into a dimensionless form as

$$\eta''(s)+2\zeta K_n\eta'(s)+K_n^2\eta(s)=\mu\lambda_1\left[1-\varepsilon\eta^2(s)\right]\eta'(s)+\mu\lambda_2\eta(s) \tag{3}$$

where $\eta = x/D$ is the dimensionless displacement, $\mu=\rho D^2L_{tip}/M$ is the mass ratio, $K_n=\rho D^2\omega_nD/M$ is the dimensionless natural frequency of the structure, and $s=Ut/D$ is the dimensionless time.

To solve Equation (3), the semi-empirical quantities λ_1, λ_2, and ε should be determined. The method proposed by Ehsan and Scanlan through fitting the envelop of experimentally measured decay-to-resonance displacement of VIV was adopted to identify these parameters in this work.[45] Firstly, Equation (3) is rearranged as

$$\eta''+K_n^2\eta=F_1(\eta,\eta') \tag{4}$$

where

$$F_1(\eta,\eta')=(\mu\lambda_1-2\zeta K_n)\eta'-\mu\lambda_1\varepsilon\eta^2\eta'+\mu\lambda_2\eta. \tag{5}$$

The solution to Equation (5) is considered to be

$$\eta(s)=A(s)\cos[K_s-\psi(s)] \tag{6}$$

where $A(s)$ and $\psi(s)$ are the time-varying VIV amplitude and phase, respectively, and $K_s=\omega_sD/U$ is the dimensionless vortex shedding frequency. Taking the derivative with respect to the dimensionless time s of Equation (6), one can obtain

$$A'(s)cos[K_s-\psi(s)]+A(s)\psi'(s)\sin[K_s-\psi(s)]=0. \tag{7}$$

Equation (7) can be rewritten as

$$A'^{(s)}=-\frac{1}{K}\left\{F_1(\eta,\eta')+A(s)\left(K^2-K_n^2\right)\cos[K_s-\psi(s)]\right\}\sin[K_s-\psi(s)], \tag{8}$$

$$\psi'^{(s)}=-\frac{1}{A(s)K}\left\{F_1(\eta,\eta')+A(s)\left(K^2-K_n^2\right)\cos[K_s-\psi(s)]\right\}\cos[K_s-\psi(s)]. \tag{9}$$

Employing the quasi-steady hypothesis and considering $A'(s)$ and $\psi'(s)$ are varying slowly with time, their averages can be treated as constants during a period of 2π, which yields

$$A'(s)=-\frac{1}{2\pi K}\int_0^{2\pi}\left[F_1(\eta,\eta')+A(s)\left(K^2-K_n^2\right)\cos p\right]\sin p dp, \tag{10}$$

$$\psi'(s)=-\frac{1}{2\pi KA(s)}\int_0^{2\pi}\left[F_1(\eta,\eta')+A(s)\left(K^2-K_n^2\right)\cos p\right]\cos p dp, \tag{11}$$

where $p = K_s - \psi(s)$. Equation (10) can be rewritten as

$$A'(s)=-\frac{1}{8}\alpha A(s)\left[A^2(s)-\beta^2\right] \tag{12}$$

where

$$\alpha=\mu\lambda_1\varepsilon, \tag{13}$$

$$\beta=\frac{2}{\sqrt{\varepsilon}}\left(1-\frac{2\zeta K_n}{\mu\lambda_1}\right)^{1/2}. \tag{14}$$

Solving Equation (12) gives

$$A(s)=\frac{\beta}{\sqrt{1-\left(\frac{A_0^2-\beta^2}{A_0^2}\right)e^{-\left(\alpha\beta^2/4\right)s}}}, \tag{15}$$

where A_0 represents the displacement amplitude in the initial place during the decay to resonance test and β is the displacement amplitude in the steady state.

Solving Equation (12) and assuming the initial phase angle equaling to zero, one can obtain $\psi(s)$ and then the dimensionless vibration displacement can be obtained as

$$\eta(s)=\frac{\beta}{\sqrt{1-\left(\frac{A_0^2-\beta^2}{A_0^2}\right)e^{-\left(\alpha\beta^2/4\right)s}}}\cos\left\{K_s-\frac{1}{2K}\left[\mu\lambda_2+\left(K^2-K_n^2\right)\right]s\right\}. \tag{16}$$

3.2 | Aero-electro-mechanical model

A typical piezoelectric energy harvester consists of a cantilever beam bonded with a piezoelectric transducer at the root to generate power, as shown in Figure 2. A circular cylinder is connected at the free end as a bluff body to induce VIV. Employing the SDOF lumped parameter model[47] to describe the energy harvesting system:

$$\begin{cases} m\ddot{x}(t)+c\dot{x}(t)+kx(t)+\theta V(t)=F_{air}(t) \\ I(t)+C_p\dot{V}(t)-\theta\dot{x}(t)=0 \end{cases}, \tag{17}$$

where $x(t)$ is the displacement of the cylinder, $V(t)$ is the output voltage of the piezoelectric sheet, m is the equivalent mass of the VIVPEH, c is the equivalent damping related to the damping ratio ζ, which can be solved by the free decay experiments, and k is the equivalent stiffness of the system. These parameters are calculated by Equation (18) where m_1 and m_2 represent the masses of the piezoelectric beam and the circular cylinder, respectively. C_p is the capacitance measured experimentally, and I represents the current flowing into the interface circuit. θ is the electromechanical coupling coefficient which could be calculated by $\theta=\sqrt{\left(\omega_{noc}^2-\omega_{nsc}^2\right)mC_p}$,[34] where ω_{noc} and ω_{nsc} are the resonant frequencies of the system under open and short-circuit conditions, respectively.

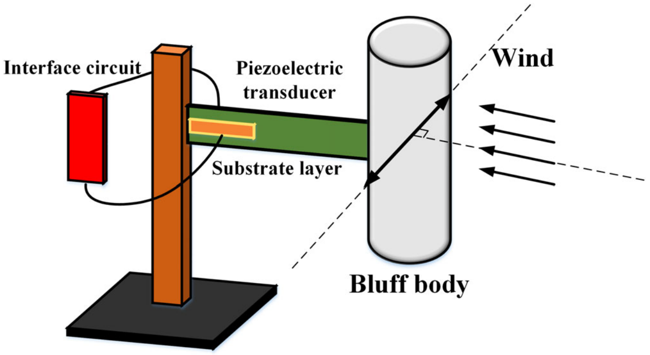

FIGURE 2 Schematic of the implementation of VIVPEH. VIV, vortex-induced vibrations; VIVPEH, VIV-based piezoelectric energy harvester [Colour figure can be viewed at wileyonlinelibrary.com]

$$\begin{cases} m = \dfrac{33}{140} m_1 + m_2 \\ c = 2m\omega_{nsc}\zeta \\ k = m\omega_{nsc}^2 \end{cases} \cdot \tag{18}$$

Combining with the Scanlan-Ehsan VIV model, the governing equations of the VIVPEH can be rewritten as

$$\begin{cases} m\ddot{x}(t) + c\dot{x}(t) + kx(t) - \theta V(t) = F_{air}(t) \\ = \dfrac{1}{2}\rho U^2 (2L_{tip}D) \left\{ \dfrac{1}{4\mu}(\alpha\beta^2 + 8\zeta K_n)\left(1 - \dfrac{\alpha}{\mu\lambda_1}\dfrac{x^2}{D^2}\right)\dfrac{\dot{x}}{D} + \dfrac{K_n^2 - K^2}{\mu}\dfrac{x}{D} \right\} \\ I(t) + C_p\dot{V}(t) + \theta\dot{x}(t) = 0 \end{cases} \cdot \tag{19}$$

3.3 | Equivalent circuit representation

A pure resistor (ie, AC interface circuit) is often used for the evaluation of the performance of energy harvesting. However, the practical energy harvesting interface circuit is much more complicated than a simple AC interface circuit. The output from the energy harvester must be rectified to a DC output first before it can be delivered to real electronics. However, the analytical formulation of a VIV-based energy harvesting system with a nonlinear sophisticated interface is cumbersome or even impossible. Thus, ECM is proposed to investigate the complex aero-electro-mechanical coupling behaviors of a VIVPEH. The aerodynamic and mechanical components are represented as equivalent electronic components based on the analogies listed in Table 1 to enable system-level simulation. The details of the analogies were presented in Tang et al.[42] The key is to properly represent the nonlinear VIV aerodynamic force in the circuit. Comparing with a harvester based on galloping, the challenge for modeling VIVPEHs lies in that the aerodynamic force is coupled with the mechanical vibration of the harvester in a nonlinear ordinary differential equation form in the traditional VIV models such as the wake oscillator model.[48] It is difficult to represent the VIV effect using a single electric component, either standard or user-defined arbitrary component. Fortunately, based on the Scanlan-Ehsan aerodynamic force model illustrated in Section 2, it is possible to model the VIV aerodynamic force in the circuit as it can be represented by a single equation. Here, we use the circuit simulator SIMetrix (SIMetrix Technologies Ltd) for simulation. Figure 3 shows the equivalent circuit of the VIVPEH system with the AC and DC interface circuits.

Equation (19) can be rewritten in an electrical form as

$$\begin{cases} L_1\ddot{q}(t) + R_1\dot{q}(t) + \dfrac{q(t)}{C_1} - NV(t) = \dfrac{1}{2}\rho U^2(2L_{tip}D) \left\{ \begin{array}{r} \dfrac{1}{4\mu}(\alpha\beta^2 + 8\zeta K_n)\left(1 - \dfrac{\alpha}{\mu\lambda_1}\dfrac{q^2(t)}{D^2}\right)\dfrac{\dot{q}(t)}{D} \\ + \dfrac{K_n^2 - K^2}{\mu}\dfrac{q(t)}{D} \end{array} \right\} \\ I(t) + C_p\dot{V}(t) + N\dot{q}(t) = 0 \end{cases} \cdot \tag{20}$$

The arbitrary source corresponding to the aerodynamic force is defined in Equation (20) as a function of the electric charge $q(t)$ and the current $\dot{q}(t)$. $q(t)$ is represented in terms of the capacitor C_1 and the associated voltage $V_{C_1}(t)$, with $q(t) = C_1 V_{C_1}(t)$. After converting into the equivalent circuit model, the nonlinear aerodynamic force on the right-hand side of Equation (19) is equivalent to a voltage source that is a function of the electric

TABLE 1 Corresponding parameters between mechanical and electrical domains

Mechanical Counterparts	Equivalent Circuit Parameters
Displacement x	Charge q
Velocity $\dot{x}(t)$	Current $\dot{q}$
Effective mass m	Inductance L_1
Effective damping c	Resistance R_1
Reciprocal of effective stiffness $1/k$	Capacitance C_1
Electromechanical coupling θ	Ideal transformer turning ratio N

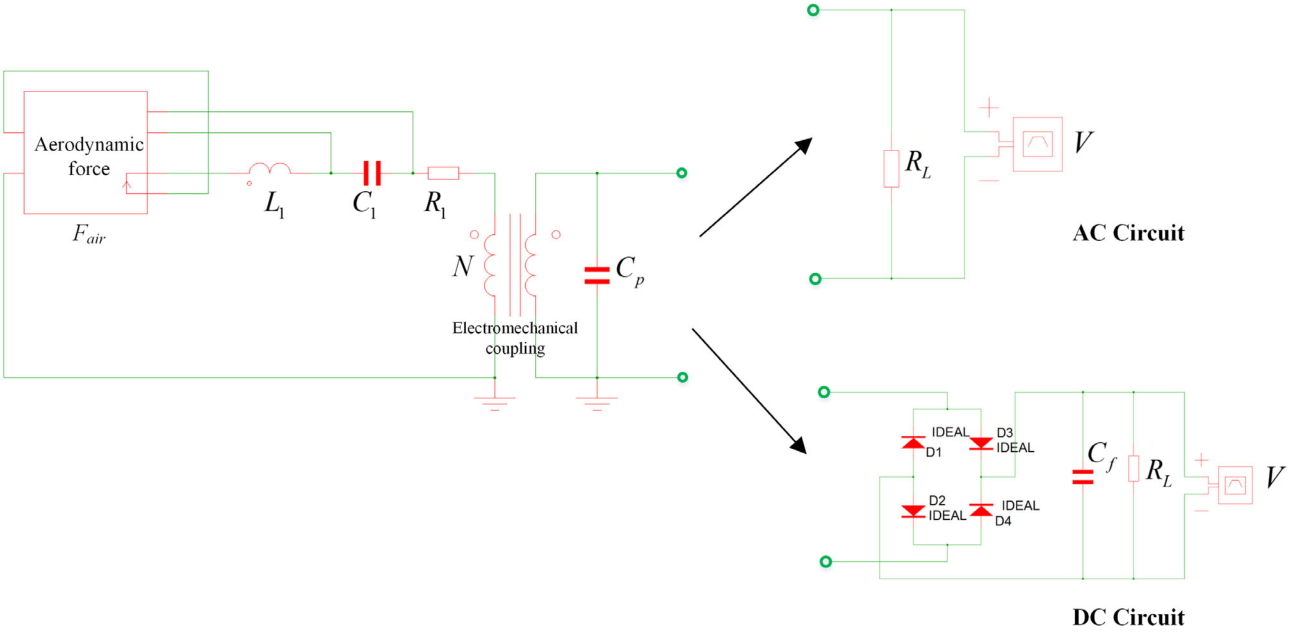

FIGURE 3 Schematic of VIVPEH system with AC and DC interface circuits. AC, alternating current; DC, direct current; VIV, vortex-induced vibrations; VIVPEH, VIV-based piezoelectric energy harvester [Colour figure can be viewed at wileyonlinelibrary.com]

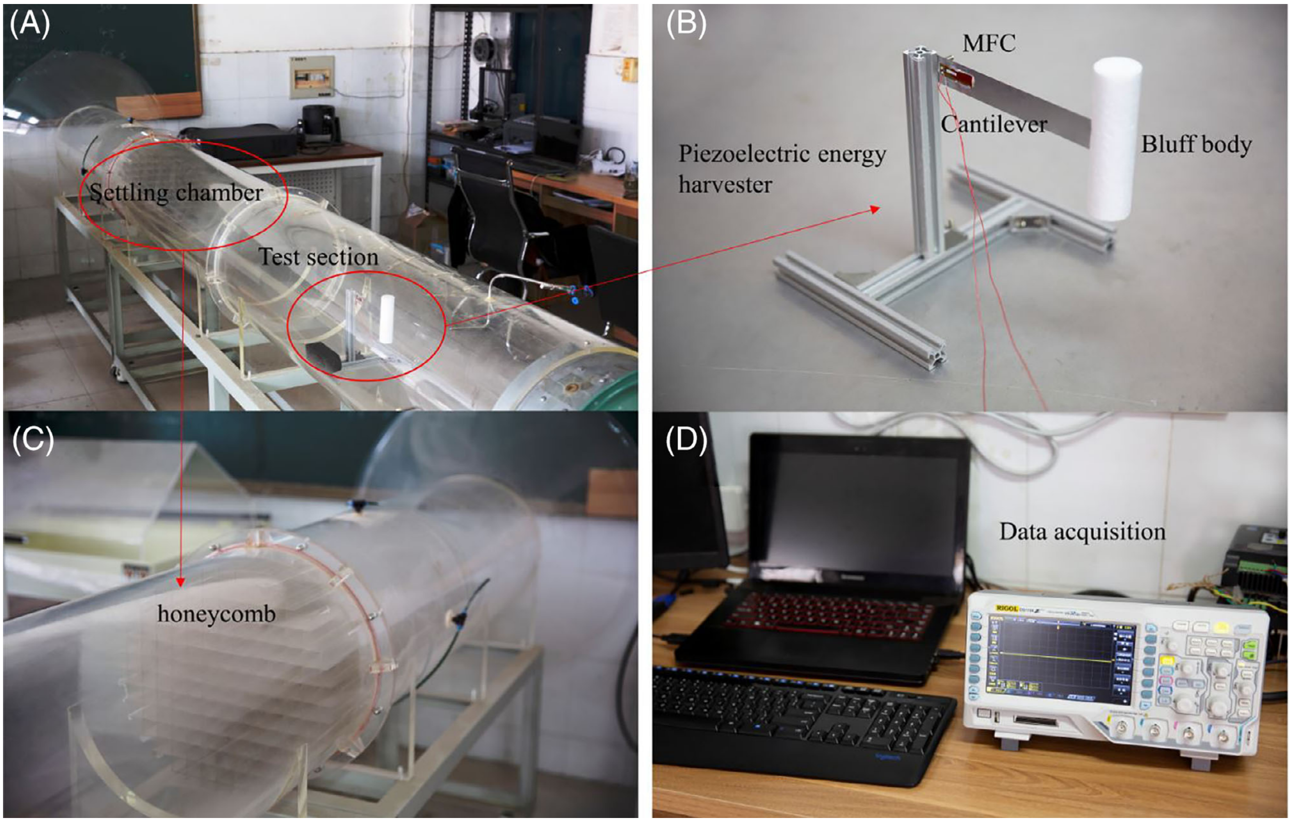

FIGURE 4 Experiments setup: A, the entire view of the wind tunnel; B, the VIVPEH; C, the settling chamber; D, the data acquisition system. VIV, vortex-induced vibrations; VIVPEH, VIV-based piezoelectric energy harvester [Colour figure can be viewed at wileyonlinelibrary.com]

charge $q(t)$ and $\dot{q}(t)$ as can be seen in Equation (20). The nonlinear transfer function provided in SIMetrix enables the user to define any arbitrary source described by an explicit expression. As shown in Figure 3, the aerodynamic force in the SIMetrix model is realized using the nonlinear transfer function denoted by a box with two input ports and one output port. One input port detects the current, that is, $\dot{q}(t)$ like an ammeter. The other one functions as a voltmeter and measures the voltage across C_1 from which one can derive $q(t)$ based on the charge-voltage-capacitance formula. The input ports do not affect the circuit behavior at all. According to the inputs and the user defined expression based on the nonlinear term, the output port produces a voltage source that will be applied to the circuit. In this way, the nonlinear relation is established in the circuit model.

Unlike the galloping-based energy harvester, the threshold wind speed of a VIVPEH is mainly controlled by the vortex shedding frequency. Since the aerodynamic coefficients for different wind speeds U are different according to the identifying process in the Scanlan-Ehsan method, the coefficients of the variables in the user-defined arbitrary source component that represents the aerodynamic force also vary with U.

4 | EXPERIMENT

A round-cross section wind tunnel is used to test the performance of the VIVPEH. As shown in Figure 4, the wind tunnel with a diameter of 400 mm can produce stable incoming flow by installing a honeycomb structure inside the settling chamber. The produced wind is with a speed in the range of $0 \leq U \leq 7$ m/s. A VIVPEH prototype is fabricated to verify the established ECM. A piezoelectric transducer (Model: MFC-2807P2, Smart Material Corp., Germany) of $37 \times 11 \times 0.6$ mm^3 is bonded on a substrate made of pure aluminum with dimensions of $200 \times 25 \times 0.5$ mm^3 to form the piezoelectric cantilever. The clamped capacitance of the piezoelectric transducer C_P is 15.7 nF. A circular-sectioned bluff body is connected at the free end of a piezoelectric cantilever, as shown in Figure 4B. The bluff body is made of hard foam with a length of 0.118 m and a diameter of 0.032 m. The damping ratio ζ of the prototyped piezoelectric cantilever can be measured from the logarithmic decrement technique. A hot-wire anemometer (Model: 405i, Testo Co, USA) is used to measure the wind speed U. The voltage output is measured by a digital oscilloscope (Model: DS1104S, RIGOL, China). Table 2 lists the parameters of the prototype in the present work.

TABLE 2 Parameters in the VIVPEH

Properties	Value
m	6.59 g
ζ	0.013
ω_n	60.288 rad/s
c	0.0098 N/m/s^{-1}
k	34.07 N/m
θ	1.9785e-5 N/V

Abbreviations: VIV, vortex-induced vibrations; VIVPEH, VIV-based piezoelectric energy harvester.

To identify the semi-empirical aerodynamic coefficients, we conduct the decay to resonance test using the wind tunnel experiments. As shown in Figure 5, assuming that the cylinder undergoes n cycles between the initial position and the threshold resonance position. To understand the effects of the aerodynamic parameters on the flow-induced vibrations, the specified parameter R_n has been introduced here:

$$R_n = \frac{A_0}{\beta}\sqrt{1-\left(\frac{A_0^2-\beta^2}{A_0^2}\right)e^{-\left(n\pi\alpha\beta^2\right)/2K}}. \tag{21}$$

Based on the deduction as mentioned above in Section 2, the relationship between the parameters α and β can be given as

$$\alpha = -\frac{2K}{n\pi\beta^2} ln\left[\frac{{A_0}^2-\beta^2{R_n}^2}{{A_0}^2-\beta^2}\right]. \tag{22}$$

Based on the results of A_0, β, and Equations (14) and (15), the aerodynamic coefficients λ_1, λ_2, and ε can be calculated as[45]

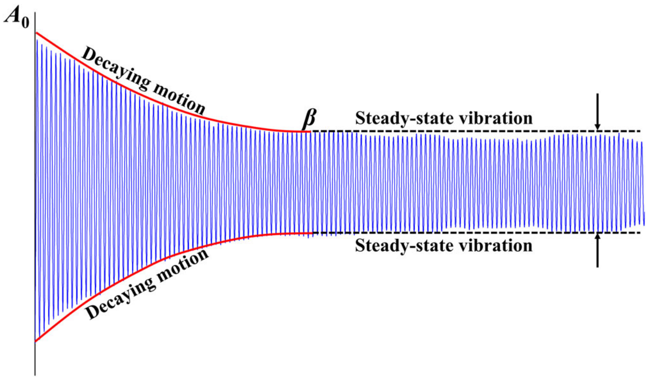

FIGURE 5 Schematic diagram of decay to resonance test under wind excitation [Colour figure can be viewed at wileyonlinelibrary.com]

$$\begin{cases} \lambda_1 = \dfrac{1}{4\mu}\left[\alpha\beta^2 + 8\zeta K_n\right] \\ \lambda_2 = \dfrac{{K_n}^2 - K^2}{\mu} \\ \varepsilon = \dfrac{\alpha}{\mu\lambda_1} \end{cases}. \tag{23}$$

Based on the above deducing process and the wind tunnel experiments, the aerodynamic coefficients can be obtained, as listed in Table 3. It is worth noting that, unlike some previous work which consider those coefficients to be constant values based on the quasi-steady theory, in the present work, the aerodynamic coefficients under every operating wind speed need to be identified seriatim respectively to make sure the reliability of the ECM.

TABLE 3 Benchmark of parameters determined by experiments

Wind Speed U, m/s	λ_1	λ_2	ε
2.098	0.1516	−0.4748	2.0451
2.235	0.1522	−0.4055	1.0956
2.372	0.1785	−0.3867	1.0991
2.509	0.1307	−0.5568	1.5158
2.646	0.1180	−0.7878	1.4419
2.783	0.1053	−0.7247	2.4348
2.920	0.0983	−0.6825	4.1341
3.057	0.0883	−0.6338	10.467

5 | RESULTS AND DISCUSSION

5.1 | Model validation

Figure 6A-D compares the experimental and predicted time history of the displacement to validate the VIV aerodynamic force model in Section 3.2. Results of four wind speed tests, that is, near the onset threshold, in the middle of the lock-in range, near the end threshold, are represented. It is seen that the predicted curves correspond quite well to the experimental curves, not only in the resonance section but also in the decay section. Thus, the identified aerodynamic force coefficients are accurately predicted and can be further used in the subsequent analysis for ECM validation and performance evaluation of the VIVPEH.

To validate the developed ECM, we further compare the voltage and output power results of the VIVPEH from experiments and ECM simulation. Figure 7A compares the measured and predicted variations of the power output with the load resistance R_L at the same wind speed U = 2.098 m/s. The average power is calculated using Joule's law in conjunction with Ohm's law: average power = RMS voltage × RMS voltage/resistive load. The effective voltage (ie, root mean square—RMS

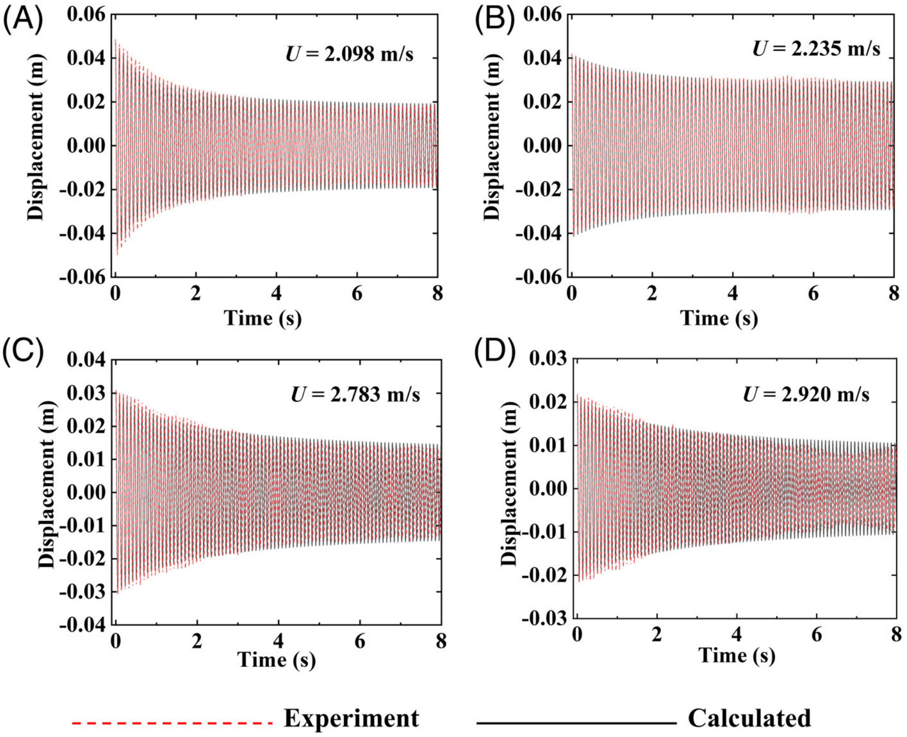

FIGURE 6 Validations of the aerodynamic coefficients of vortex-induced vibration: A, U = 2.098 m/s; B, U = 2.235 m/s; C, U = 2.783 m/s; D, U = 2.920 m/s [Colour figure can be viewed at wileyonlinelibrary.com]

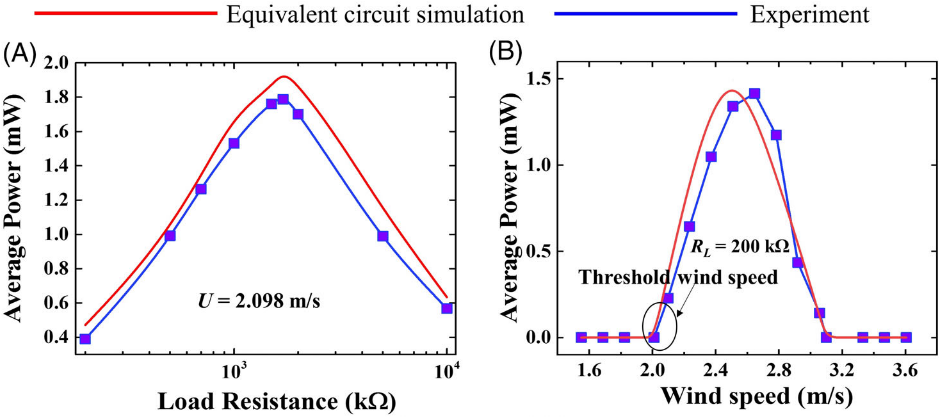

FIGURE 7 Validation of the ECM: variations of average power with A, load resistance and B, wind speed. ECM, equivalent circuit model [Colour figure can be viewed at wileyonlinelibrary.com]

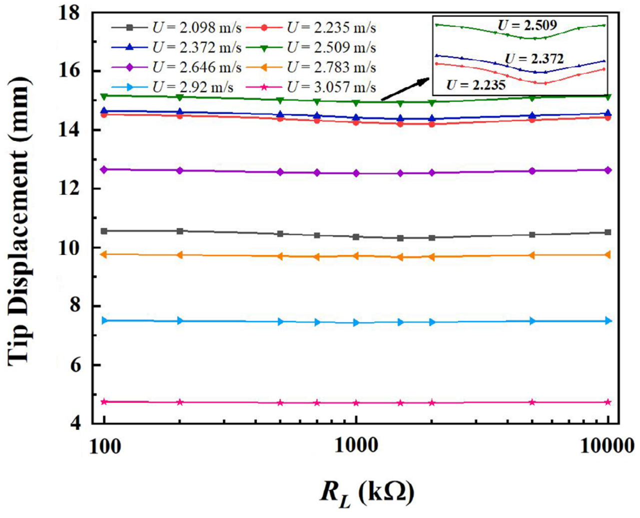

FIGURE 8 Tip displacement with AC circuit with various RL. AC, alternating current [Colour figure can be viewed at wileyonlinelibrary.com]

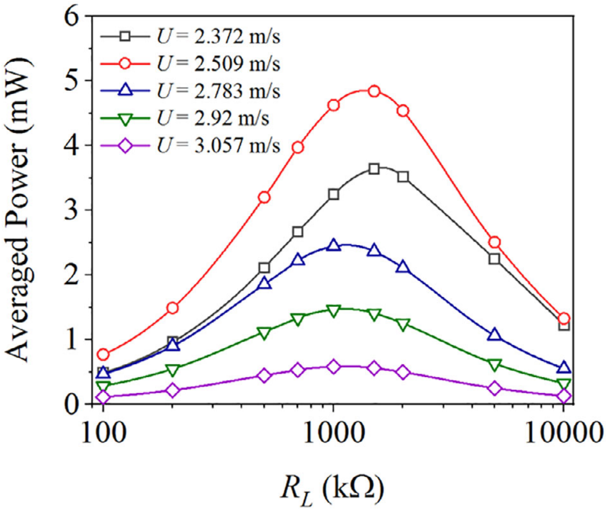

FIGURE 9 Power output with AC circuit vs RL with various U. AC, alternating current [Colour figure can be viewed at wileyonlinelibrary.com]

voltage) equals the value of the direct voltage that would produce the same power dissipation in the same resistive load during a cycle. For an alternating electric voltage with a pure since waveform, it is well known that the RMS voltage is equal to the voltage amplitude divided by $\sqrt{2}$. There exists an optimal load resistance at about $R_L = 1.5\,\text{M}\Omega$ for both the ECM prediction and experiment. The measured maximum power output is slightly lower than the ECM prediction. The probable reason of the discrepancy could be that the aerodynamic force of the vortex-induced vibrations in the circuit simulation model is established with the lumped parameter model. In Figure 7B, with $R_L = 200$ kΩ, the variations of the voltage with the wind speed of the VIVPEH are compared. The simulation results of the lock-in region and the maximum voltage value agree well with the experimental measurements. From the above comparisons, both the Scanlan-Ehsan aerodynamic force model and the equivalent circuit model are validated.

5.2 | Performance comparison with different circuits

5.2.1 | AC circuit

Based on the ECM validated in this work, we conduct further investigation on the performance of the VIVPEH with different circuits. First, an AC circuit interface is considered. Figure 8 shows the influence of the load resistance R_L on the peak tip displacement of the VIVPEH at different wind speeds. For wind speeds near the onset and ending thresholds, the displacement amplitudes are relatively small. The electrical damping effect induced by R_L seems quite weak, as the displacement curves are quite flat. For wind speeds in the middle of the lock-in region, that is, U= 2.509 m/s, 2.372 m/s, and 2.235 m/s, it can be observed that there exist valleys in the response curves, which are more obvious in the partially enlarged figure. The maximum electrical damping is induced near $R \approx 1.5\ \text{M}\Omega$, reflecting the maximum decline of the amplitude. The highest amplitude of the vibrations occurs at $U = 2.509$ m/s, which is about three times higher than the minimum value.

Figure 9 compares the average power output vs R_L for different wind speeds. There exists an optimal R_L for each wind speed. The optimal loads are slightly different for different wind speeds. This is because in the present aerodynamic model, the nonlinear aerodynamic force damping coefficients vary with U, which influences the vibrations and thus the power performance of the energy harvester. At $U = 2.509$ m/s, the highest power is obtained. At this wind speed, the limit-cycle oscillations of the VIVPEH are fully developed. For $U = 3.057$ m/s, the vibration is struggling out of the lock-in region, and the amplitude gets lower. Figure 10 further compares the power output vs wind speed with different values of R_L. The lock-in phenomenon can be found in all the cases. At a constant wind speed, the average power firstly increases and then decreases with R_L. A maximum power output of 4.839 mW is obtained at $R_L = 1.5\ \text{M}\Omega$ and $U \approx 2.5$ m/s.

5.2.2 | DC circuit

The performance of the VIVPEH with DC circuit has been investigated with the ECM in this part. For such a case, it is quite challenging to derive the analytical or numerical solution. As shown in Figure 3, the circuit includes a full-wave rectifier, a filtering capacitor C_{filter}, and a resistor R_L. C_{filter} is set to be an appropriately considerable value to make sure the voltage across R_L smooth and quasi-constant when the VIVPEH is operating in the steady state. Figure 11 shows the displacement vs R_L with different wind speeds. The variation trend of the displacement with a DC circuit is similar to that with AC circuit. However, in the enlarged figure, the displacement valleys at $U = 2.235$ m/s, 2.372 m/s, and 2.509 m/s are shallower than the case with the AC interface. This shows that the electrical damping produced by the AC interface is higher than that of the DC interface.

Figures 12 and 13 depict the responses of the average power output with different R_L and U. The variation of

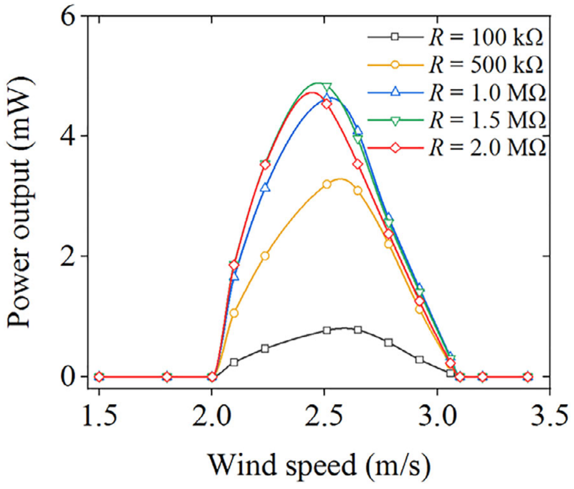

FIGURE 10 Power output with AC circuit vs U with various RL. AC, alternating current [Colour figure can be viewed at wileyonlinelibrary.com]

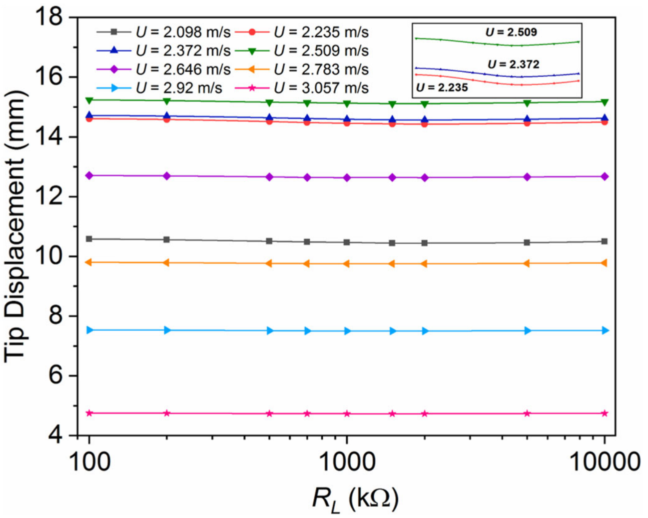

FIGURE 11 Tip displacement with a standard DC interface at different RL. DC, direct current [Colour figure can be viewed at wileyonlinelibrary.com]

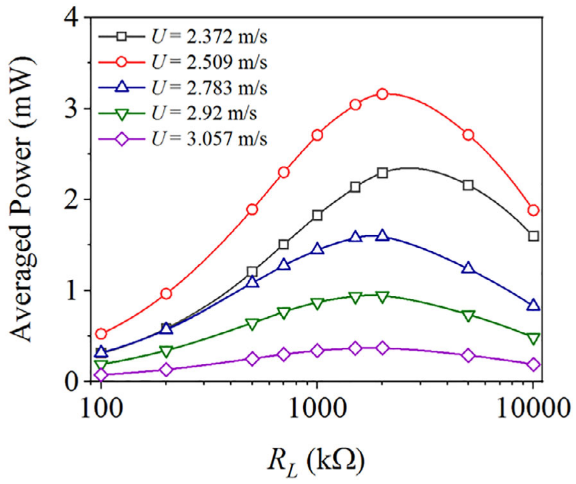

FIGURE 12 Power output with DC circuit vs RL with various U. DC, direct current [Colour figure can be viewed at wileyonlinelibrary.com]

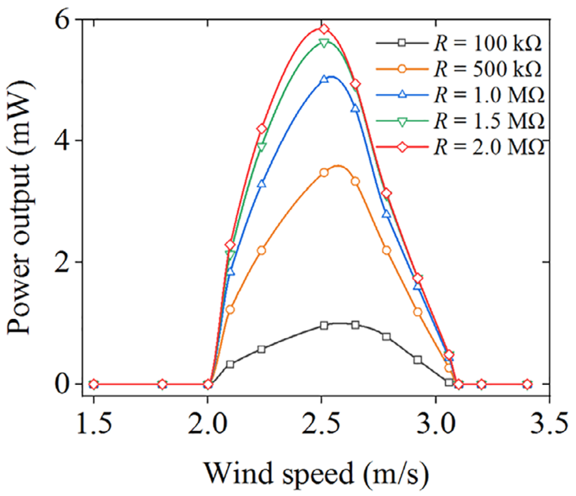

FIGURE 13 Power output with DC circuit vs U with various RL. DC, direct current [Colour figure can be viewed at wileyonlinelibrary.com]

power response has a similar trend as that with an AC interface, that is, it firstly increases with R_L up to $R_L = 1.1$ M and then decreases, which is for the reason that the electrical energy generated inside the piezoelectric sheets is being scavenged in a whole period of the vibrations all the time for the AC circuit while for the DC circuit. Energy scavenging stops when the voltage across C_{filter} is higher than the voltage developed on the piezoelectric sheets. Firstly, with a standard DC interface, the average power output of the VIVPEH is lower than that with the AC interface. The maximum power output of 5.84 mW occurs at $R_L = 2$ MΩ and $U = 2.509$ m/s. The optimal load resistance also changes slightly comparing with the ac case.

6 | CONCLUSIONS

This paper presents an effective approach to describe the mechanism of the VIVPEH system basing on equivalent circuit representation. The aerodynamic force based on the Scanlan-Ehsan vortex-induced force model which acts as the user-defined electronic component is presented. The mechanical parameters and piezoelectric coupling in the system are represented by the standard electronic components. System-level simulation and performance analysis can be realized based on the established ECM of the entire system of VIVPEH. Aerodynamic wind tunnel tests are firstly conducted to verify the accuracy of Scanlan-Ehsan aerodynamic model, and then experiment on the evaluation of energy harvesting performance is conducted to validate the proposed approach. A parametric study has been presented to examine the performance of the VIVPEH with different AC and DC circuits, including the power output, the electrical damping, and the vibration displacement. Important conclusions based on the system-level analysis and simulation are given as

1. Average power output: For the two interfaces, the maximum power output occurs in the full resonance region of the lock-in region with a specific load R_L. The harvested power with the AC interface is higher than that with the DC interface at the optimal load.
2. Induced electrical damping: For the two interfaces, the highest electrical damping leads to the valley in the Power output vs load resistance response at particular constant wind speed. Particularly, the DC interface induces smaller electrical damping than the AC interface, corresponding to the higher optimal power output.

It is worth mentioning that the parametric study is performed under relatively low electromechanical coupling condition. In future work, the influence of different electromechanical coupling strength on VIVPEH will be further investigated.

ACKNOWLEDGEMENTS

The authors gratefully acknowledge the support provided by the National Natural Science Foundation of China (No. 51606171, 51977196, 51705296, and 51708011), China Postdoctoral Science Foundation (No. 2019M652565), and Blue Sky Grant 2019 of the University of Technology Sydney (321720.2232432).

ORCID

Lihua Tang https://orcid.org/0000-0001-9031-4190
Liya Zhao https://orcid.org/0000-0002-6229-4871
Guobiao Hu https://orcid.org/0000-0002-1288-7564

REFERENCES

1. Zou H, Zhao L, Gao Q, et al. Mechanical modulations for enhancing energy harvesting: principles, methods and applications. *Appl Energy*. 2019;255:113871.
2. Zhao L, Zou H, Yan G, et al. Magnetic coupling and flextensional amplification mechanisms for high-robustness ambient wind energy harvesting. *Energ Conver Manage*. 2019;201:112166.
3. Huang D, Zhou S, Han Q, Litak G. Response analysis of the nonlinear vibration energy harvester with an uncertain parameter. *Proceedings of the Institution of Mechanical Engineers, Part K: Journal of Multi-Body Dynamics*. 2019. https://doi.org/10.1177/1464419319893211.
4. Fan K, Liang G, Zhang Y, Tan Q. Hybridizing linear and nonlinear couplings for constructing two-degree-of-freedom electromagnetic energy harvesters. *International Journal of Energy Research*. 2019;43:8004-8019.
5. Sun W, Guo F, Seok J. Development of a novel vibro-wind galloping energy harvester with high power density incorporated with a nested bluff-body structure. *Energ Conver Manage*. 2019;197:111880.

6. Ma Y, Luan Y, Xu W. Hydrodynamic features of three equally spaced, long flexible cylinders undergoing flow-induced vibration. *European Journal of Mechanics, B/Fluids*. 2020;79:386-400.
7. Yang K, Wang J, Yurchenko D. A double-beam piezo-magneto-elastic wind energy harvester for improving the galloping-based energy harvesting. *Appl Phys Lett*. 2019;115(19):193901.
8. Shan X, Li H, Yang Y, Feng J, Wang Y, Xie T. Enhancing the performance of an underwater piezoelectric energy harvester based on flow-induced vibration. *Energy*. 2019;172:134-140.
9. Aquino AI, Calautit JK, Hughes BR. Evaluation of the integration of the wind-induced flutter energy harvester (WIFEH) into the built environment: experimental and numerical analysis. *Appl Energy*. 2017;207:61-77.
10. Shan X, Tian H, Chen D, Xie T. A curved panel energy harvester for aeroelastic vibration. *Appl Energy*. 2019;249:58-66.
11. Hu G, Wang J, Su Z, Li G, Peng H, Kwok K. Performance evaluation of twin piezoelectric wind energy harvesters under mutual interference. *Appl Phys Lett*. 2019;115(7):073901.
12. Sun W, Jo S, Seok J. Development of the optimal bluff body for wind energy harvesting using the synergetic effect of coupled vortex induced vibration and galloping phenomena. *International Journal of Mechanical Sciences*. 2019;156:435-445.
13. He, X., Yang, X., and Jiang, S., "Enhancement of wind energy harvesting by interaction between vortex-induced vibration and galloping"., *Appl Phys Lett*. 112(3): p. 033901 (2018).
14. Bernitsas MM. OMAE06-92645 VIVACE (vortex induced vibration for aquatic clean energy): a new concept in generation of clean and renewable energy from fluid flow. *Journal of Offshore Mechanics & Arctic Engineering*. 2008;130(4):619-637.
15. Raghavan, K. and Bernitsas, M.M., "Enhancement of high damping VIV through roughness distribution for energy harnessing at 8×103 < Re < 1.5×105", (48234): p. 871–882 (2008).
16. Fan K, Liu S, Liu H, Zhu Y, Wang W, Zhang D. Scavenging energy from ultra-low frequency mechanical excitations through a bi-directional hybrid energy harvester. *Appl Energy*. 2018;216:8-20.
17. Lai Z, Wang J, Zhang C, Zhang G, Yurchenko D. Harvest wind energy from a vibro-impact DEG embedded into a bluff body. *Energ Conver Manage*. 2019;199:111993.
18. Yurchenko D, Lai Z, Thomson G, Val DV, Bobryk RV. Parametric study of a novel vibro-impact energy harvesting system with dielectric elastomer. *Appl Energy*. 2017;208:456-470.
19. Wu Y, Hu Y, Huang Z, Lee C, Wang F. Electret-material enhanced triboelectric energy harvesting from air flow for self-powered wireless temperature sensor network. *Sensors and Actuators A: Physical*. 2018;271:364-372.
20. Hou C, Chen T, Li Y, et al. A rotational pendulum based electromagnetic/triboelectric hybrid-generator for ultra-low-frequency vibrations aiming at human motion and blue energy applications. *Nano Energy*. 2019;63:103871.
21. Zou H, Zhang Y, Guo L, et al. Quantifying the triboelectric series. *Nat Commun*. 2019;10(1):1427.
22. Liang J, Liao WH. Improved design and analysis of self-powered synchronized switch interface circuit for piezoelectric energy harvesting systems. *IEEE Transactions on Industrial Electronics*. 2011;59(4):1950-1960.
23. Wu Y, Qiu J, Zhou S, Ji H, Chen Y, Li S. A piezoelectric spring pendulum oscillator used for multi-directional and ultra-low frequency vibration energy harvesting. *Appl Energy*. 2018;231:600-614.
24. Mei X, Zhou S, Yang Z, et al. A tri-stable energy harvester in rotational motion: Modeling, theoretical analyses and experiments. *Journal of Sound and Vibration*. 2020;469:115142.
25. Huang D, Zhou S, Yang Z. Resonance mechanism of nonlinear vibrational multistable energy harvesters under narrow-band stochastic parametric excitations. *Complexity*. 2019;20:1050143.
26. Zhang G, Zhang X, Wang D, et al. Performance evaluation and operation optimization of the steam ejector based on modified model. *Applied Thermal Engineering*. 2019;163:114388.
27. Chen Z, He J, Wang G. Vibration bandgaps of piezoelectric metamaterial plate with local resonators for vibration energy harvesting. *Shock and Vibration*. 2019;2019:1397123.
28. Hu Y, Luo A, Wang J, Wang F. Voltage regulation and power management for wireless flow sensor node self-powered by energy harvester with enhanced reliability. *IEEE Access*. 2019;7:154836-154843.
29. Wang J, Hu G, Su Z, et al. A cross-coupled dual-beam for multi-directional energy harvesting from vortex induced vibrations. *Smart Materials and Structures*. 2019;28:12LT02.
30. Wang J, Tang L, Zhao L, Zhang Z. Efficiency investigation on energy harvesting from airflows in HVAC system based on galloping of isosceles triangle sectioned bluff bodies. *Energy*. 2019;172:1066-1078.
31. Dai HL, Abdelkefi A, Wang L. Theoretical modeling and nonlinear analysis of piezoelectric energy harvesting from vortex-induced vibrations. *Journal of Intelligent Material Systems and Structures*. 2014;25(14):1861-1874.
32. Mehmood A, Abdelkefi A, Hajj MR, Nayfeh AH, Akhtar I, Nuhait AO. Piezoelectric energy harvesting from vortex-induced vibrations of circular cylinder. *J Sound Vib*. 2013;332(19):4656-4667.
33. Zhou S, Wang J. Dual serial vortex-induced energy harvesting system for enhanced energy harvesting. *AIP Advances*. 2018;8(7):075221.
34. Wang J, Zhou S, Zhang Z, Yurchenko D. High-performance piezoelectric wind energy harvester with Y-shaped attachments. *Energ Conver Manage*. 2019;181:645-652.
35. Liu W, Badel A, Formosa F, Zhu Q, Zhao C, Hu G-D. A comprehensive analysis and modeling of the self-powered synchronous switching harvesting circuit with electronic breakers. *IEEE Transactions on Industrial Electronics*. 2018;65(5):3899-3909.
36. Liu W, Yuan Z, Zhang S, Zhu Q. Enhanced broadband generator of dual buckled beams with simultaneous translational and torsional coupling. *Appl Energy*. 2019;251:113412.
37. Lien I, Shu Y. Array of piezoelectric energy harvesting by the equivalent impedance approach. *Smart Materials and Structures*. 2012;21(8):082001.
38. Aghakhani A, Basdogan I. Equivalent impedance electroelastic modeling of multiple piezo-patch energy harvesters on a thin plate with AC–DC conversion. *IEEE/ASME Transactions on Mechatronics*. 2017;22(4):1575-1584.
39. Yang Y, Tang L. Equivalent circuit modeling of piezoelectric energy harvesters. *Journal of Intelligent Material Systems & Structures*. 2009;20(18):2223-2235.
40. Bayik B, Aghakhani A, Basdogan I, Erturk A. Equivalent circuit modeling of a piezo-patch energy harvester on a thin plate

with AC–DC conversion. *Smart Materials and Structures*. 2016; 25(5):055015.
41. Silva TM, Clementino MA, Erturk A, De Marqui Jr C. Equivalent electrical circuit framework for nonlinear and high quality factor piezoelectric structures. *Mechatronics*. 2018;54: 133-143.
42. Tang L, Zhao L, Yang Y, Lefeuvre E. Equivalent circuit representation and analysis of galloping-based wind energy harvesting. *IEEE/ASME Transactions on Mechatronics.* 2014;20 (2):834-844.
43. Zhao L, Yang Y. Comparison of four electrical interfacing circuits in wind energy harvesting. *Sensors and Actuators A: Physical*. 2017;261:117-129.
44. Zhao L, Tang L, Liang J, Yang Y. Synergy of wind energy harvesting and synchronized switch harvesting interface circuit. *IEEE/ASME Transactions on Mechatronics*. 2017;22(2): 1093-1103.
45. Ehsan F, Scanlan RH. Vortex-induced vibrations of flexible bridges. *J Eng Mech*. 1990;116(6):1392-1411.
46. Zou Q, Ding L, Wang H, Wang J, Zhang L. Two-degree-of-freedom flow-induced vibration of a rotating circular cylinder. *Ocean Eng*. 2019;191:106505.
47. Erturk A, Inman DJ. Issues in mathematical modeling of piezoelectric energy harvesters. *Smart Materials and Structures.* 2008;17(6):065016.
48. Facchinetti ML, De Langre E, Biolley F. Coupling of structure and wake oscillators in vortex-induced vibrations. *Journal of Fluids and Structures*. 2004;19(2):123-140.

How to cite this article: Wang J, Tang L, Zhao L, Hu G, Song R, Xu K. Equivalent circuit representation of a vortex-induced vibration-based energy harvester using a semi-empirical lumped parameter approach. *Int J Energy Res*. 2020;1–13. https://doi.org/10.1002/er.5228